NASA TECHNICAL NOTE

NASA TN D-8270

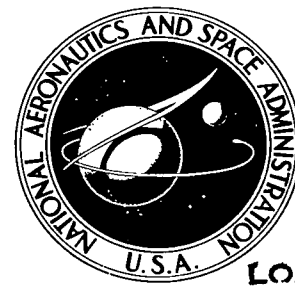

NASA TN D-8270

EXPERIMENTAL DYNAMIC STIFFNESS AND DAMPING OF EXTERNALLY PRESSURIZED GAS-LUBRICATED JOURNAL BEARINGS

David P. Fleming, William J. Thayer, and Robert E. Cunningham

Lewis Research Center
and U.S. Army Air Mobility R&D Laboratory
Cleveland, Ohio 44135

NATIONAL AERONAUTICS AND SPACE ADMINISTRATION • WASHINGTON, D. C. • JUNE 1976

1. Report No. NASA TN D-8270	2. Government Accession No.	3. Recipient's Catalog No.
4. Title and Subtitle EXPERIMENTAL DYNAMIC STIFFNESS AND DAMPING OF EXTERNALLY PRESSURIZED GAS-LUBRICATED JOURNAL BEARINGS		5. Report Date June 1976 6. Performing Organization Code
7. Author(s) David P. Fleming, William J. Thayer, and Robert E. Cunningham		8. Performing Organization Report No. E-8636 10. Work Unit No. 505-04
9. Performing Organization Name and Address NASA Lewis Research Center and U.S. Army Air Mobility R&D Laboratory Cleveland, Ohio 44135		11. Contract or Grant No. 13. Type of Report and Period Covered Technical Note
12. Sponsoring Agency Name and Address National Aeronautics and Space Administration Washington, D.C. 20546		14. Sponsoring Agency Code

15. Supplementary Notes

16. Abstract

A rigid vertical shaft was operated with known amounts of unbalance at speeds to 30 000 rpm and gas supply pressure ratios to 4.8. From measured amplitude and phase angle data, dynamic stiffness and damping coefficients of the bearings were determined. The measured stiffness was proportional to the supply pressure, while damping was little affected by supply pressure. Damping dropped rapidly as the fractional frequency whirl threshold was approached. A small-eccentricity analysis overpredicted the stiffness by 20 to 70 percent. Predicted damping was lower than measured at low speeds but higher at high speeds.

17. Key Words (Suggested by Author(s)) Gas bearings Externally pressurized bearings Dynamic bearing properties	18. Distribution Statement Unclassified - unlimited STAR Category 37

19. Security Classif. (of this report)	20. Security Classif. (of this page)	21. No. of Pages	22. Price*
Unclassified	Unclassified	28	$4.00

* For sale by the National Technical Information Service, Springfield, Virginia 22161

EXPERIMENTAL DYNAMIC STIFFNESS AND DAMPING OF EXTERNALLY PRESSURIZED GAS-LUBRICATED JOURNAL BEARINGS

by David P. Fleming, William J. Thayer, and Robert E. Cunningham

Lewis Research Center and
U. S. Army Air Mobility R&D Laboratory

SUMMARY

Experiments were conducted to determine the dynamic properties of 63-millimeter-diameter, externally pressurized gas journal bearings. A rigid vertical shaft was operated with known amounts of unbalance to produce a rotating load on the bearings. Speeds ranged to 30 000 rpm and gas supply pressure ratios to 4.8. Measurements were made of the amplitude of the synchronous shaft whirling and of the phase angle between the shaft displacement and the unbalance vector. From these data, dynamic stiffness and damping coefficients of the bearings were determined.

The measured stiffness was proportional to the supply pressure, while damping was little affected by supply pressure. Damping dropped rapidly as the fractional frequency whirl threshold was approached. Increasing the amount of unbalance increased the damping but decreased the stiffness.

A small-eccentricity analysis overpredicted the stiffness by some 20 percent at the highest supply pressures and up to 70 percent at the lowest supply pressures. Predicted damping was lower than measured at low speeds but higher at high speeds.

INTRODUCTION

Externally pressurized, gas-lubricated bearings are attractive for a number of applications. They offer the advantages of self-acting gas bearings - cleanliness, freedom from oil systems, easily met sealing requirements - plus a much higher load capacity and some freedom from the fractional frequency whirl which often plagues self-acting gas bearings.

Gas-lubricated bearings are often used in high-speed applications. Thus a knowledge of the bearing's dynamic properties is necessary in order to design the rotor-

bearing system to avoid excessive amplitudes of rotor motion. Previous work at Lewis Research Center (refs. 1 and 2) measured the steady-state properties of orifice-compensated, gas-lubricated journal bearings. Further work (ref. 3) determined that experimental zero-speed stiffness data could be satisfactorily used to predict rotor rigid-body critical speeds.

The amplitude of rotor motion in response to unbalance excitation depends heavily on bearing damping, especially near the critical speeds. Damping cannot be determined from steady-state unidirectional-load data, and attempts to use analytical bearing properties to determine rotor critical speeds and amplitudes have not been notably successful (ref. 4).

The objectives of the investigation reported herein were to experimentally determine the dynamic stiffness and damping of a 63-millimeter-diameter, externally pressurized gas journal bearing. The exciting force was that of a known unbalance applied to the rotor; thus the bearing was subjected to a load which rotated at rotor speed. This is the predominant load in many types of high-speed machinery. Bearing properties were measured for supply pressure ratios to 4.8, speeds to 30 000 rpm, and unbalance eccentricities to 16 percent of the bearing clearance. The results were compared with the predictions of a small-eccentricity analysis.

The data were taken in the U.S. customary system of units and converted to SI units for reporting purposes.

APPARATUS

The apparatus used in this investigation was basically the same as that used in references 1 and 2; it is shown in figure 1. Two bronze test bearings were mounted in stainless steel plates. Three vertical arbors, with appropriate spacers, located the bearing plates with a span of 203 millimeters. The bearing plates could be moved relative to each other to aline the two bearings. The rotor was oriented vertically; its weight was supported by an externally pressurized thrust bearing. The rotor was driven by pressurized air from two nozzles impinging on 30 buckets milled in the rotor at the upper end. An identical set of buckets at the lower end (cut in the opposite direction) was used for braking. The photograph in figure 1 shows a pneumatic load cylinder and loader bearing, used in obtaining the data of references 1 and 2. These devices were not used in the present work; no external loads were applied to the rotor.

One of the externally pressurized bearings is shown, along with the test rotor, in figure 2. Each bearing was 63 millimeters in diameter by 95 millimeters long, giving a length-to-diameter ratio of 1.5. The bearings were made of cast aluminum bronze and were precision machined before installation in the apparatus. Geometry gage measurements of the bores showed roundness and concentricity to be within 1 micrometer. The

two bearings had slightly different diameters, resulting in radial clearances of 39.1 micrometers in the upper bearing and 37.6 micrometers in the lower.

Each bearing had 12 orifice plugs arranged in two rows of six equally spaced around the circumference. The orifice planes were located one-quarter of the way in from the bearing ends. Figure 3 shows the orifice mounting method. The orifices were set back 0.76 millimeter from the bearing surface. The ratio of orifice recess volume to bearing lubricant volume (given by πDLC) was thus 0.1. (All symbols are defined in the appendix.) The inherent compensation factor a^2/dC for this bearing was 0.7, making the bearing predominantly orifice compensated.

The rotor was 63 millimeters in diameter and 460 millimeters long. It was made of SAE 52100 steel and weighed 11.1 kilograms. Measurement of the rotor showed it to be round within 0.5 micrometer and concentric within 1.3 micrometer over the bearing lengths. The rotor was drilled radially in four places at each end. Into these holes were inserted set screws. These were used to dynamically balance the rotor and also to insert a known unbalance, which applied a rotating load to the bearings.

INSTRUMENTATION

Two orthogonally mounted capacitance distance probes were mounted outboard of each bearing (fig. 1). These probes provided a noncontacting method of monitoring rotor displacement. Each probe was calibrated before installation in the test apparatus. The sensitivity of the probes with their displacement meters was nominally 1 volt per 0.25 millimeter.

Rotor speed was measured by an inductive sensor close to the turbine buckets and displayed in rpm on a digital counter. The speed was also measured with a photodiode, which viewed the periphery of the shaft at the upper end. The shaft in this area was painted a flat black over half of the circumference; the other half was the bare, finely ground shaft surface. Thus the output of the photodiode was a square wave with 1 cycle per shaft revolution. This signal served as a phase reference, as well as a speed measurement.

The remainder of the instrumentation conditioned the signals from the noncontact probes and photodiode and yielded output in terms of rotor amplitude and phase angle. Figure 4 schematically depicts the instruments.

The photodiode output, a square wave whose frequency equals the rotor speed, was used as one input to a phase meter. The signal was also fed into a dynamic input sine converter (DISC). The DISC had two outputs: The first was a d.c. signal proportional to rotor speed, which was input to the x-axis of the XYY plotter. The second was a sine wave of the same frequency as the square wave input. The sine wave signal passed into a carrier generator whose output was one input of a tracking filter. The other tracking

filter input was the amplified signal from a selected capacitance probe. The filter output, then, was the synchronous component of the capacitance probe signal, that is, the synchronous component of the rotor motion. This signal was passed to a peak-to-peak voltmeter whose output was one of the Y inputs of the XYY plotter. The filtered amplitude signal was also input to the phase meter, along with the photodiode square wave. The phase meter output was a d.c. voltage proportional to the phase angle between the square wave and the rotor amplitude sine wave. Phase angle was read directly on a digital voltmeter and also provided the second Y input to the XYY plotter. Thus the plotter provided graphs of rotor amplitude and phase angle as functions of rotor speed.

The capacitance probe signals were also connected, in orthogonal pairs, to an X-Y curve-tracing oscilloscope. In this way the rotor orbit could be observed visually and any nonsynchronous motion readily detected.

TEST PROCEDURE

Prior to the first test run, the upper bearing was carefully alined with respect to the lower. Precision gage measurements showed the bearing axes to be alined within 2 micrometers radially and 10 microradians angularly. The rotor was balanced in place by means of the set screws installed in the rotor (fig. 1). The amplitude of rotor motion after balancing did not exceed 0.22 micrometer. There was no noticeable buildup at the known critical speed, indicating that the observed amplitude was chiefly due to runout. Measured critical-speed amplitudes were 8 to 100 times the balanced amplitude; thus the error due to residual runout is small.

For the test runs the rotor was unbalanced by turning in one balancing screw at each end of the rotor to provide excitation for a translatory whirl. All instruments were turned on and allowed to warm up. Air was then supplied to the rotor drive turbine, and the rotor accelerated slowly to the maximum speed for the particular test conditions. (This was usually the speed at which fractional frequency whirl became apparent, as indicated on the oscilloscope presentation.) The turbine drive air was then shut off and the rotor allowed to coast down in speed. During coastdown, rotor amplitude and phase angles for one bearing were plotted as functions of speed on the XYY plotter. Two coastdowns were thus needed to obtain data for both bearings; these were usually made on the same sheet of graph paper. A typical plot is shown as figure 5.

DATA REDUCTION

Once the rotor amplitudes and phase angles are determined, it is necessary to

translate them into bearing stiffness and damping coefficients. This is done by inverting the equations of motion of a rigid rotor, as found in reference 5. The following assumptions were made prior to inverting the equations of motion:

(1) The shaft unbalance is known exactly. This unbalance is placed in the shaft in-line and in-phase, such that the mass axis of the shaft parallels the geometric axis. Since the rotor mass center is midway between the bearings, this means that any conical motion of the rotor is due to slight differences between the two bearings.

(2) The bearings are isotropic, such that any point in the shaft makes a circular orbit about the axis defined by the bearing centers. With this condition, it is not possible to distinguish between direct and cross-coupled bearing coefficients. For convenience, only the direct coefficients will be retained in the equations of motion. These are

$$K_i = K_{ix} = K_{iy}$$

$$B_i = B_{ix} = B_{iy}$$

The equations of motion then became

$$\frac{M}{S}(T_2\ddot{x}_1 - T_1\ddot{x}_2) + K_1x_1 + K_2x_2 + B_1\dot{x}_1 + B_2\dot{x}_2 = (U_1 + U_2)\omega^2 \cos \omega t \tag{1}$$

$$\frac{M}{S}(T_2\ddot{y}_1 - T_1\ddot{y}_2) + K_1y_1 + K_2y_2 + B_1\dot{y}_1 + B_2\dot{y}_2 = (U_1 + U_2)\omega^2 \sin \omega t \tag{2}$$

$$\frac{I_t}{S}(\ddot{x}_2 - \ddot{x}_1) + \frac{I_p\omega}{S}(\dot{y}_2 - \dot{y}_1) + B_2T_2\dot{x}_2 + B_1T_1\dot{x}_1 + K_2T_2x_2 + K_1T_1x_1 = (U_1\rho_1 + U_2\rho_2)\omega^2 \cos \omega t \tag{3}$$

$$\frac{I_t}{S}(\ddot{y}_2 - \ddot{y}_1) - \frac{I_p\omega}{S}(\dot{x}_2 - \dot{x}_1) + B_2T_2\dot{y}_2 + B_1T_1\dot{y}_1 + K_2T_2y_2 + K_1T_1y_1 = (U_1\rho_1 + U_2\rho_2)\omega^2 \sin \omega t \tag{4}$$

Figure 6 illustrates the notation of these equations.

The rotor coordinates at the bearings may be expressed as

$$x_i = E_i \cos \omega t + F_i \sin \omega t \tag{5}$$

$$y_i = -F_i \cos \omega t + E_i \sin \omega t \tag{6}$$

These expressions are differentiated to obtain the shaft velocity and acceleration, and

the results are substituted into equations (1) to (4).

Equation (1) may now be multiplied by $\cos \omega t$ and equation (2) by $\sin \omega t$ and the resulting equations added. Similarly, equation (1) may be multiplied by $\sin \omega t$ and equation (2) by $\cos \omega t$ and one equation subtracted from the other. The results of the addition and subtraction are independent of time and may be written

$$-\frac{M}{S}\omega^2(T_2E_1 - T_1E_2) + K_1E_1 + K_2E_2 + \omega B_1F_1 + \omega B_2F_2 = (U_1 + U_2)\omega^2 \tag{7}$$

$$-\frac{M}{S}\omega^2(T_2F_1 - T_1F_2) + K_1F_1 + K_2F_2 - \omega B_1E_1 - \omega B_2E_2 = 0 \tag{8}$$

Equations (3) and (4) may be treated similarly, the results being

$$\frac{\omega^2}{S}(I_t - I_p)(E_1 - E_2) + T_2K_2E_2 + T_1K_1E_1 + T_2\omega B_2F_2 + T_1\omega B_1F_1 = (U_1\rho_1 + U_2\rho_2)\omega^2 \tag{9}$$

$$\frac{\omega^2}{S}(I_t - I_p)(F_1 - F_2) + T_2K_2F_2 + T_1K_1F_1 - T_2\omega B_2E_2 - T_1\omega B_1E_1 = 0 \tag{10}$$

Equations (7) to (10) constitute four equations in the unknowns K_1, K_2, B_1, and B_2; they may be readily solved simultaneously.

It must be noted at this point that the displacement probes are not at the bearing centers but outboard of the bearings. Furthermore, measurements are made on the test apparatus in terms of amplitude and phase angle. Thus, rotor x-direction motion at a probe is given by

$$\xi_i = A_i \cos(\omega t - \varphi_i) \tag{11}$$

This may also be expressed in the form of equation (5) as

$$\xi_i = G_i \cos \omega t + H_i \sin \omega t$$

If $\cos(\omega t - \varphi_i)$ is expanded, one sees that

$$G_i = A_i \cos \varphi_i$$

$$H_i = A_i \sin \varphi_i$$

As x and y components of amplitude vary linearly along the rotor, E and F may be expressed in terms of G and H:

$$E_i = G_1 + \frac{G_2 - G_1}{\zeta_2 - \zeta_1}(z_i - \zeta_1)$$

$$F_i = H_1 + \frac{H_2 - H_1}{\zeta_2 - \zeta_1}(z_i - \zeta_1)$$

Since the z-coordinate is measured from the lower bearing, $z_1 = 0$ and $z_2 = L$.

The preceding calculations are all carried out by a computer. The computer program accepts as input the amplitude and phase angle at the probes and the rotor speed.

It was recognized that amplitudes at the two bearings might not always be equal, thus introducing some cocking of the rotor in the bearings. Accordingly, the misalinement, as a fraction of the bearing clearance, was calculated for each test point by the formula

$$q = [(x_1 - x_2)^2 + (y_1 - y_2)^2]^{1/2} \frac{L}{SC}$$

As used here, then, q is a measure of the clearance change over the length of the bearing. For the present experiments, the average value of q was 1.5 percent; the maximum was 6 percent. Thus, any effect of misalinement on bearing performance should be small.

ERROR ANALYSIS

The dynamic characteristics of a gas film, specifically stiffness and damping, cannot be measured directly. Values of these coefficients must be calculated from the values that can be measured directly - these being displacement, phase angle, frequency, and initial clearance.

A number of different sensors and instruments are necessary to measure these variables and, of course, each is subject to error. Typical accuracies of instruments used as obtained from manufacturers' operating manuals (ref. 6) are shown in table I. Which instruments are involved in each measurement may be determined from figure 4. Table II summarizes the errors involved. In computing the possible error in phase angle, any phase shifts in the various instruments involved have been neglected.

In addition to the instrument errors, there are inaccuracies in determining the applied unbalance (0.13 percent) and rotor mass (0.1 percent), in reading the plotted results (0.25 percent in speed, 0.5 percent in amplitude, and 1 percent in phase angle for midrange values), and because of the residual runout (0.22 μm in amplitude at an unknown phase angle).

The possible errors in the direct measurements must now be translated into the

resultant errors in bearing stiffness and damping. As it is very difficult to write explicit expressions for stiffness and damping for the actual four-degree-of-freedom system, a two-degree-of-freedom model has been used for the error computation. This corresponds exactly to the actual system when the rotor motion is purely cylindrical. The stiffness and damping may then be written

$$K = \omega^2 \left[U \cos \frac{\varphi}{A} + M \right]$$

$$B\omega = \omega^2 U \sin \frac{\varphi}{A}$$

In these expressions, K and B denote the total stiffness and damping for both bearings, and U is the total unbalance. The error expressions are obtained by differentiation:

$$\frac{dK}{K} = \frac{2|d\omega|}{\omega} + \frac{U\omega^2}{AK}\left[\left(\frac{|dU|}{U} + \frac{|dA|}{A}\right)|\cos \varphi| + |\sin \varphi \, d\varphi|\right] + \left(\frac{\omega}{\omega_{cr}}\right)^2 \frac{|dM|}{M}$$

$$\frac{dB\omega}{B\omega} = \frac{2|d\omega|}{\omega} + \frac{|dU|}{U} + \frac{|dA|}{A} + |\cot \varphi \, d\varphi|$$

These equations show that the resultant errors in stiffness and damping depend not only on measurement errors, but also on the phase angle between the unbalance and the response. The most accurate results are generally obtained near resonance.

Sample error results, calculated for the run with a pressure ratio of 4.8 and 66 g mm unbalance, show that the possible error in stiffness is 2.6 percent at resonance, 5 percent when $\varphi = 135^\circ$, and 16 percent when φ reaches 180°. For damping, the possible error is 12 percent at resonance and 15 percent when $\varphi = 135^\circ$ and becomes unbounded as φ approaches 180°. The probable errors, of course, are less, as some cancellation of errors is likely to occur.

RESULTS

Bearing dynamic stiffness and damping are plotted as functions of rotor speed in figures 7 to 10. The (a) and (b) parts of each figure show stiffness, and the (c) and (d) parts show damping. Conversely, the (a) and (c) parts are for the upper bearing, and the (b) and (d) parts for the lower bearing. Each figure is for one bearing supply pressure ratio, with two or three curves for different amounts of unbalance. The unbalances applied were 10, 52, and 66 g mm total for the rotor. This corresponds to mass eccentricities of approximately 2.5, 13, and 16 percent of the bearing clearance. These

unbalances produced maximum critical-speed rotor amplitudes of 13, 50, and 58 percent of the bearing clearance. For a given unbalance, critical-speed amplitude increased with supply pressure.

Also shown in each plot are theoretical predictions. These have been computed from the analysis of reference 7 by taking the whirl frequency equal to the rotative frequency (synchronous whirl). Since this is a small eccentricity perturbation analysis, one curve applies to all unbalance levels. The correction factor of Lund (ref. 8) was applied to account for there being only six orifices per row rather than the line source assumed by reference 7.

Figure 7 is for a supply pressure ratio of 2.3; that is, the absolute supply pressure was 2.3 times the ambient pressure. For this case the stiffness is nearly constant with speed. Increasing the unbalance from 10 to 52 g mm results in a small decrease in stiffness over most of the speed range. The maximum bearing eccentricity ratio for this supply pressure was 0.25; thus the bearing was always operating in the "small eccentricity" region. The upper bearing shows somewhat higher stiffness than the lower bearing. This is contrary to expectation, since the clearance of the upper bearing was slightly larger (39.1 μm versus 37.6 μm). This ranking of the two bearings was the same for all but the highest pressure ratio used.

The analysis predicted considerably higher stiffness than observed. This is possibly due to the non-line-source correction factor being inadequate for the small number of orifices actually used (6 per plane).

Bearing damping generally rises with speed, except for the upper bearing at 10 g mm unbalance. For this case, damping is nearly constant over most of the speed range, decreasing near the highest speed tested. Damping is higher with a larger unbalance. The predicted damping is lower than measured at low speeds but approaches the measured values at high speeds. It may be noted in figure 7(d) that the measured and predicted curves have nearly the same slope at low speeds.

Figure 8, for a pressure ratio of 3.0, is generally similar to figure 7 as regards stiffness. However, for the lower bearing, the stiffness initially decreases with speed and then increases. For the higher unbalance (52 g mm) the lower bearing stiffness again drops at the highest speeds tested. The stiffness values are higher than those of figure 7, as expected for an externally pressurized bearing.

Bearing damping initially increases with speed and then decreases. The decrease is pronounced in the upper bearing with the lower unbalance level (10 g mm) and appears to signal the approach of the fractional frequency whirl threshold, which imposed an upper limit to rotor speed. Predicted damping values are lower than measured at low speeds but become higher at high speed. (The predicted values do not consider the proximity of the fractional frequency whirl threshold.) In contrast to the stiffness, the overall damping level was changed little by increasing the supply pressure. In common with figure 7, increasing the unbalance increases the damping but decreases the stiffness.

Figure 9 is for a pressure ratio of 3.5. This figure is generally similar to figure 8 for a pressure ratio of 3.0.

Figure 10, for a pressure ratio of 4.8, has curves for three unbalance levels. In addition to unbalances of 10 and 52 g mm, as in the previous figures, an unbalance of 66 g mm was used. The stiffness curves for the three unbalance levels are somewhat more widely separated than at the lower pressure ratios. Conversely, the damping curves are grouped closer together. As expected, the stiffness is the highest observed in this series of runs, while damping values are nearly the same as for lower supply pressures.

Some general observations can now be made. Table III shows the average stiffness of the lower bearing over the speed range as a function of the pressure ratio and the unbalance level. As observed previously, stiffness rises with pressure ratio and falls with increasing unbalance. The small influence of speed is shown by the rms deviation from the average, which appears in the fourth column of table III. The deviation has been listed in the form $\sigma_k/\overline{K}$ converted to percent, where σ_k is the rms deviation and $\overline{K}$ the average stiffness. The largest deviation is 4 percent. This verifies the visual observation that the influence of speed is minimal.

The last column in table III shows the stiffness in the dimensionless form $C\overline{K}/(p_s - p_a)LD$. For the three higher supply pressures, the dimensionless stiffness is nearly constant, indicating that dimensional stiffness is proportional to the gage supply pressure.

The critical speed has been marked by a solid circle on the curves of figures 7 to 10. This is the speed where the amplitude is highest. The critical speed increases with increasing supply pressure and decreases with increasing unbalance. This behavior is reasonable, since higher supply pressure increased the bearing stiffness, while higher unbalance reduced the stiffness. The relation of supply pressure, measured stiffness, damping, critical speed, and calculated critical speed is shown in table IV. The measured values shown are the averages for the two bearings. The peak amplitude for the lower bearing generally occurred at a slightly higher speed. The last column of table IV shows the critical speed calculated by the formula

$$\omega_{cr} = \left[\frac{\frac{\overline{K}}{M}}{1 - \frac{1}{2}\left(\frac{B\omega}{\overline{K}}\right)^2} \right]^{1/2}$$

where the quantities on the right side are taken at the measured critical speed. The formula was derived by finding the speed at which the response of a damped system is maximized (ref. 9). The measured and calculated critical speeds agree closely, the average deviation being just over 2 percent.

The predicted stiffness is consistently less than that measured. The disparity ranges from 20 percent at the high supply pressures to 70 percent at the low pressures. This follows the trend observed in reference 1 for steady-state data. As mentioned earlier, this may be due to inadequate theoretical treatment of the small number of orifices used; the theory was developed for a line source with a correction factor applied to account for the actual finite number of orifices.

The analysis of Majumdar (ref. 10), which accounts for the effects of individual orifices, showed better agreement with the experimental data of reference 1 than did the analysis of Fleming, et al. (ref. 7). Majumdar's results unfortunately have not been published for the case of synchronous whirling. An additional factor not accounted for in either analysis is the pressure recovery which occurs downstream of the orifice.

A further difference between theory and experiment is the behavior with changing speed. The measured stiffness remained relatively constant as the speed changed, while the predicted stiffness increased with speed. This difference also occurred for some of the steady-state results in reference 1.

An interesting observation in this regard is the theoretical behavior as the speed and whirl ratio are changed. In this report the theoretical stiffness has been taken from the radial load component of the bearing f_r when the bearing whirls at its rotational speed. Under this condition, f_r increases with speed. The behavior is similar when there is no whirl, that is, under a steady load. However, at the critical frequency for fractional frequency whirl (usually slightly over half the rotational frequency), f_r is equal to or less than its value at zero speed. That is, there is no increase with rotational speed. This is, for most of the data, exactly the behavior observed experimentally under conditions of synchronous whirl. The zero-speed predictions appear as horizontal dashed lines in the (a) and (b) parts of figures 7 to 10. Agreement with experiment is better than are the actual-speed predictions, both in magnitude and in trend with changing speed.

The overall magnitude of damping was changed little by supply pressure. Maximum damping generally occurred near the critical speed. Thus, for higher supply pressures, the maximum damping occurred at higher speeds, and the damping curves are more "spread out" in speed. Above the critical speed, and particularly near the fractional frequency whirl threshold, damping decreased rapidly. Predicted damping values were conservative at low speeds but were higher than measured values at higher speeds. As previously mentioned, the analysis does not consider the mass supported by the bearing and its effect on critical speeds or fractional frequency whirl thresholds.

SUMMARY OF RESULTS

Experiments were conducted with externally pressurized, gas-lubricated journal

bearings to determine the dynamic stiffness and damping during synchronous whirl. The whirl orbit was produced by a deliberately unbalanced rotor. Supply pressure ratios to 4.8, rotor speeds to 30 000 rpm, and unbalance eccentricities to 16 percent of the bearing clearance were investigated. The following results were obtained:

1. Stiffness increased with supply pressure and decreased with increasing unbalance. Measured stiffness was approximately proportional to the gage supply pressure. There was little variation of stiffness with speed.

2. Damping was little affected by supply pressure, except as increasing supply pressure increased the critical speed. Damping generally increased with increasing speed below the rotor critical speed and then decreased. A larger unbalance resulted in increased damping.

3. Stiffness was overestimated by small-eccentricity perturbation theory. The theory also predicted increasing stiffness with speed, which was not observed experimentally. The predicted stiffness for the case of no rotation agreed better with experiment than the actual-speed predictions throughout the speed range.

4. Predicted damping was lower than observed at low speeds and higher at high speeds. The disparity at high speeds is probably because the theory does not consider the fractional frequency whirl threshold.

Lewis Research Center,
National Aeronautics and Space Administration,
and
U.S. Army Air Mobility R&D Laboratory,
Cleveland, Ohio, April 6, 1976,
505-04.

APPENDIX - SYMBOLS

A	rotor amplitude, m
a	orifice radius, m
B	bearing damping coefficient, N-sec/m
C	bearing radial clearance, m
D	bearing diameter, m
d	orifice recess diameter, m
E, F	amplitude components of rotor motion at bearings, m
f_r	theoretical radial load component of bearing, N
G, H	amplitude components of rotor motion at probes, m
I_p	rotor polar moment of inertia, kg m^2
I_t	rotor transverse moment of inertia, kg m^2
K	bearing dynamic stiffness, N/m
$\overline{K}$	bearing dynamic stiffness averaged over speed range, N/m
L	bearing length, m
M	rotor mass, kg
P_s	supply pressure ratio p_s/p_a
p_a	atmospheric pressure, Pa
p_s	absolute supply pressure, Pa
q	misalinement fraction, dimensionless
S	bearing span, m
T_i	distance from rotor mass center to bearing i (measured in +z direction), m
t	time, sec
U	unbalance, kg m
x_i, y_i	rotor coordinates at bearing i, m
z	rotor axial coordinate measured from lower bearing, m
ζ_i	z-coordinate of probe i, m
ξ_i	rotor x-direction coordinate at probe i, m
ρ_i	distance from rotor mass center to unbalance i (measured in +z direction), m

σ_k rms deviation of stiffness from average value, N/m

φ phase angle, rad

ω rotor angular speed, rad/sec

Subscripts:

cr critical speed

i bearing, probe, or unbalance i

x, y x or y directions

REFERENCES

1. Cunningham, Robert E.; Fleming, David P.; and Anderson, William J.: Experiments on Rotating Externally Pressurized Air Journal Bearings. I - Load Capacity and Stiffness. NASA TN D-5191, 1969.

2. Cunningham, Robert E.; Fleming, David P.; and Anderson, William J.: Experiments on Rotating Externally Pressurized Air Journal Bearings. II - Attitude Angle and Air Flow. NASA TN D-5192, 1969.

3. Cunningham, Robert E.; and Gunter, Edgar J., Jr.: Critical Speeds of a Rotor in Rigidly Mounted, Externally Pressurized, Air-Lubricated Bearings. NASA TN D-6350, 1971.

4. Dayton, R. D.; and Chasman, M. R.: Experimental Rotor Unbalance Response Using Hydrostatic Lubrication. J. Lubric. Technol., Trans. ASME, Ser. F, vol. 95, no. 4, Oct. 1973, pp. 469-477.

5. Gunter, Edgar J., Jr.; and DeChoudhury, P.: Rigid Rotor Dynamics. NASA CR-1391, 1969.

6. Cunningham, Robert E.: Experimentally Determined Stiffness and Damping of an Inherently Compensated Air Squeeze-Film Damper. NASA TN D-7987, 1975.

7. Fleming, David P.; Cunningham, Robert E.; and Anderson, William J.: Stability Analysis for Unloaded Externally Pressurized Gas-Lubricated Bearings with Journal Rotation. NASA TN D-4934, 1968.

8. Lund, J. W.: A Theoretical Analysis of Whirl Instability and Pneumatic Hammer for a Rigid Rotor in Pressurized Gas Journal Bearings. J. Lubric. Technol., Trans. ASME, Ser. F, vol. 89, no. 2, Apr. 1967, pp. 154-166.

9. Thomson, William T.: Mechanical Vibrations. 2nd ed., Prentice-Hall, Inc., 1953, p. 85.

10. Majumdar, B. C.: Analysis of Externally Pressurized Gas Bearings with Journal Rotation. Wear, vol. 24, 1973, pp. 15-22.

TABLE I. - TYPICAL INSTRUMENT ACCURACIES

[From ref. 6.]

	Error, percent
Proximity sensor output	±2.6
Digital voltmeter	±3.0
Amplifier	±.01
Dynamic input sine converter	±.25
Tracking filter	±2.0
Phase meter	.08
Peak-to-peak d.c. voltmeter	±4.0
XYY plotter	±.2

TABLE II. - INSTRUMENTATION ERRORS IN DIRECT MEASUREMENTS

Reading					
Speed		Amplitude		Phase angle	
Contribution to error	Error, percent	Contribution to error	Error, percent	Contribution to error	Error, percent
DISC	0.25	Capacitance probe	2.6	Phase meter	0.08
Plotter	.2	Amplifier	.01	Amplifier	.01
		Tracking filter	2.0	Plotter	.2
		Peak-to-peak voltmeter	4.0		
		Plotter	.2		
Total possible error, percent	0.45		8.8		0.3

TABLE III. - AVERAGE DYNAMIC STIFFNESS OF LOWER BEARING

Pressure ratio, P_s	Unbalance, U, g mm	Average stiffness, $\overline{K}$, MN/m	rms Deviation, $\sigma_k/\overline{K}$, percent	Dimensionless stiffness, $C\overline{K}/(p_s - p_a)LD$
2.3	10	8.3	4	0.40
	52	8.1	1	.39
3.0	10	14.6	3	.46
	52	13.9	4	.44
3.5	10	19.1	2	.48
	52	18.9	2	.47
4.8	10	29.7	2	.49
	52	27.7	3	.46
	66	26.4	3	.43

TABLE IV. - CRITICAL-SPEED PROPERTIES

Pressure ratio, P_s	Unbalance, U, g mm	Measured stiffness, K, MN/m	Measured damping, $B\omega$, MN/m	Measured critical speed, rpm	Calculated critical speed, rpm
2.3	10	8.7	4.8	13 700	13 000
2.3	52	8.6	5.3	13 600	13 200
3.0	10	14.8	5.2	16 700	16 100
3.0	52	14.8	5.9	16 600	16 300
3.5	10	19.2	5.4	18 700	18 100
3.5	52	18.7	6.6	18 300	18 100
4.8	10	28.9	5.7	22 300	22 000
4.8	52	26.3	7.0	21 600	21 200
4.8	66	25.3	7.4	21 100	20 800

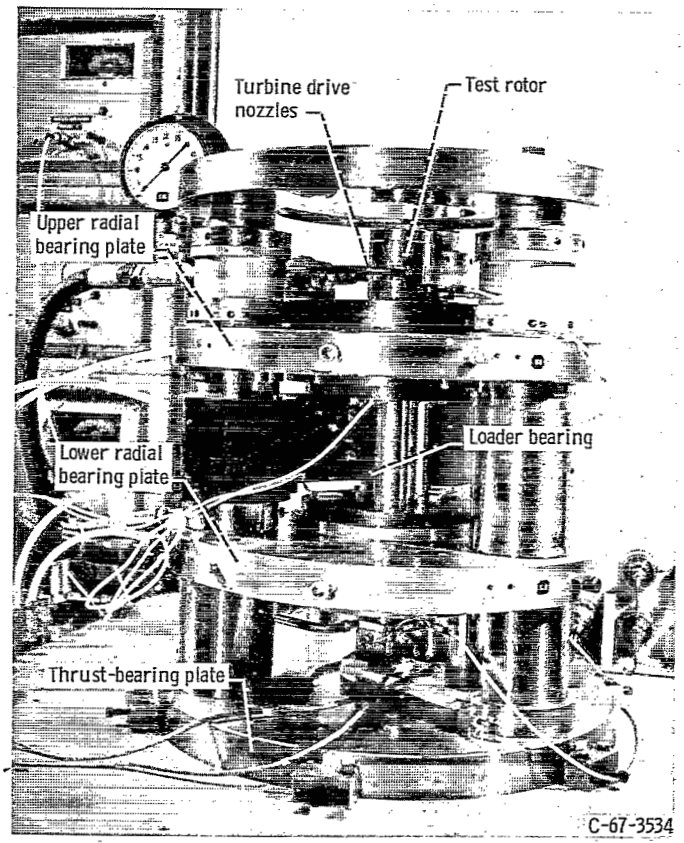

Figure 1. - Externally pressurized air bearing test apparatus.

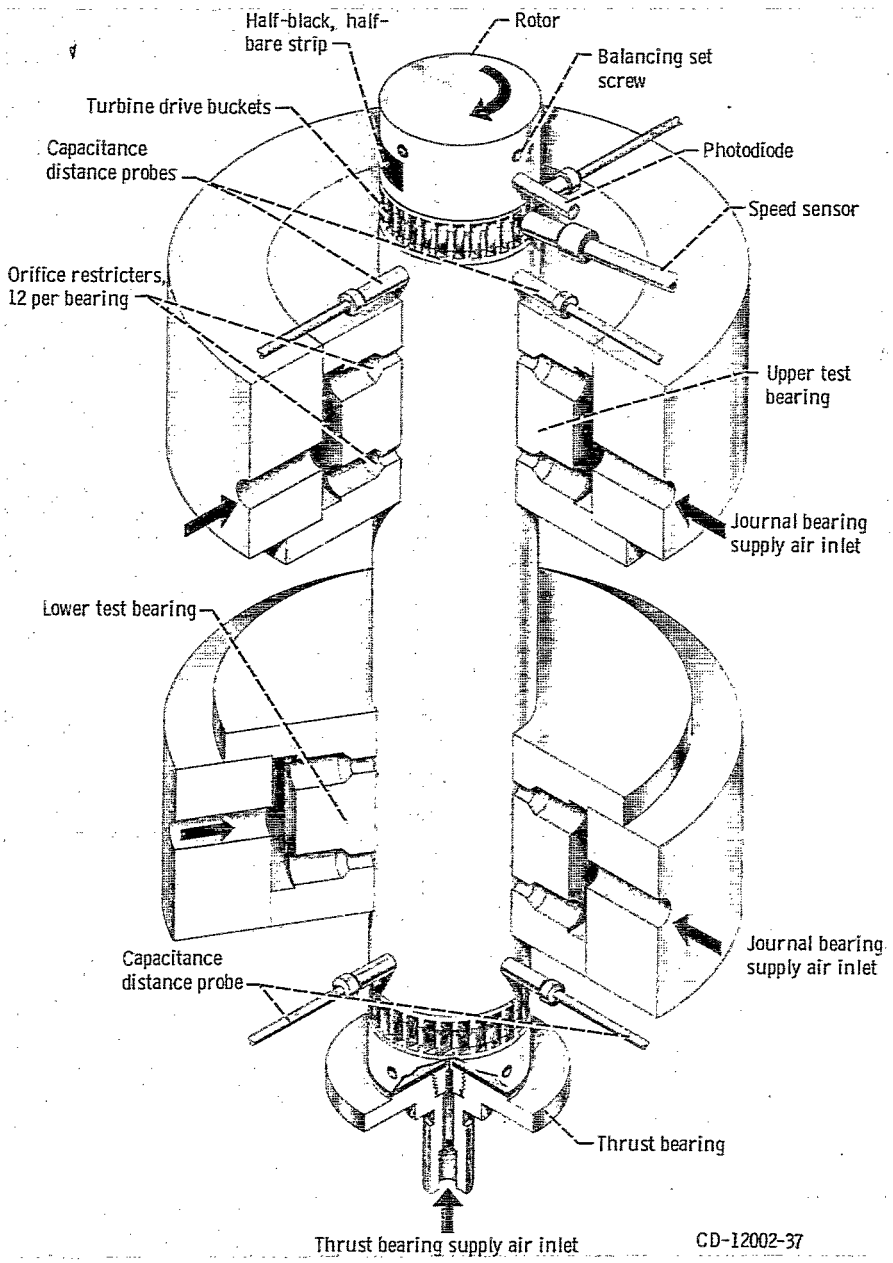

Figure 1. - Concluded.

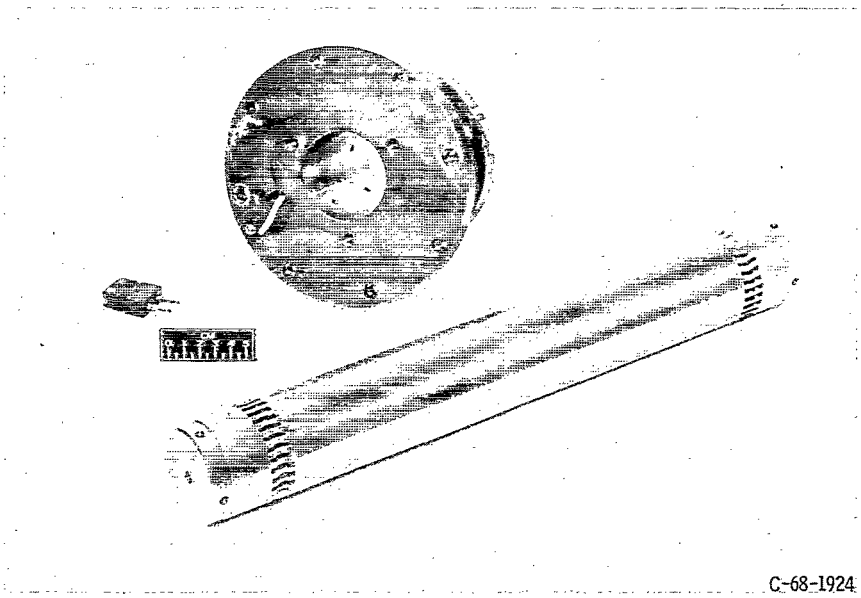

C-68-1924

Figure 2. - Test bearing and rotor.

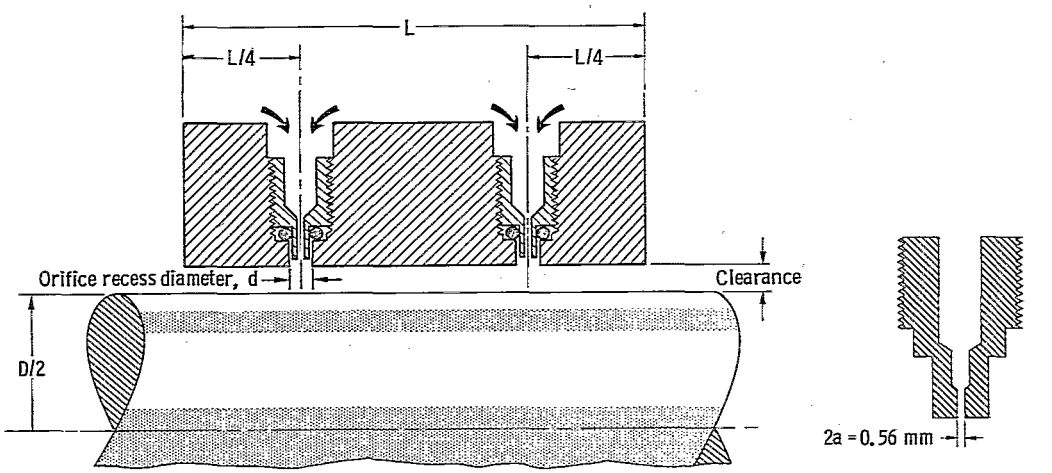

CD-9940-15

(a) Method of orifice mounting.

(b) Orifice detail.

Figure 3. - Section view of test bearing.

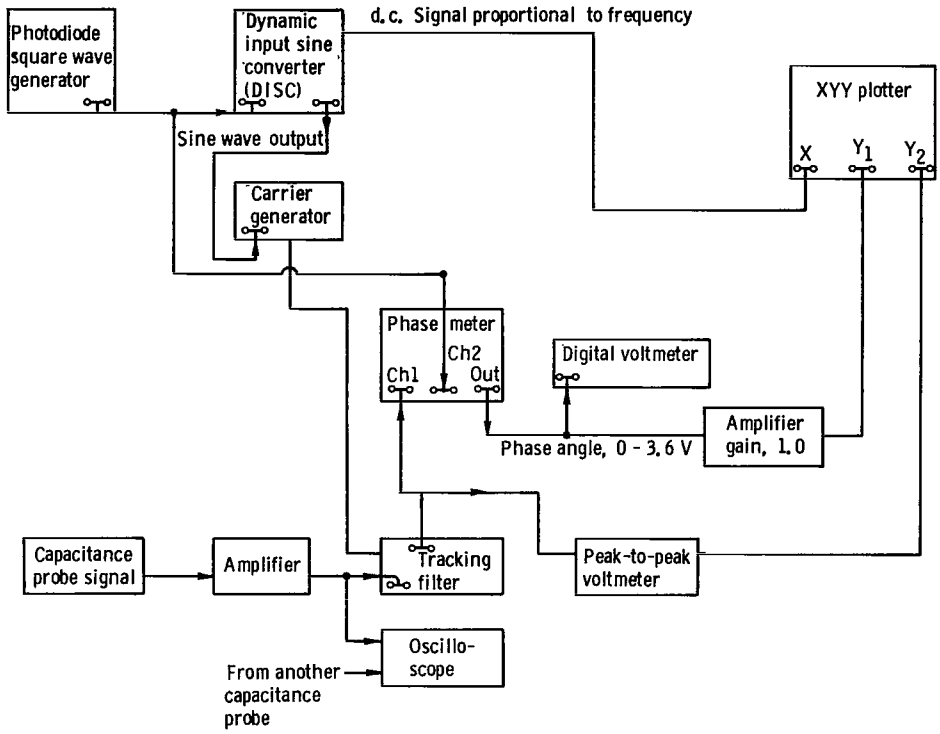

Figure 4. - Schematic diagram of instrumentation.

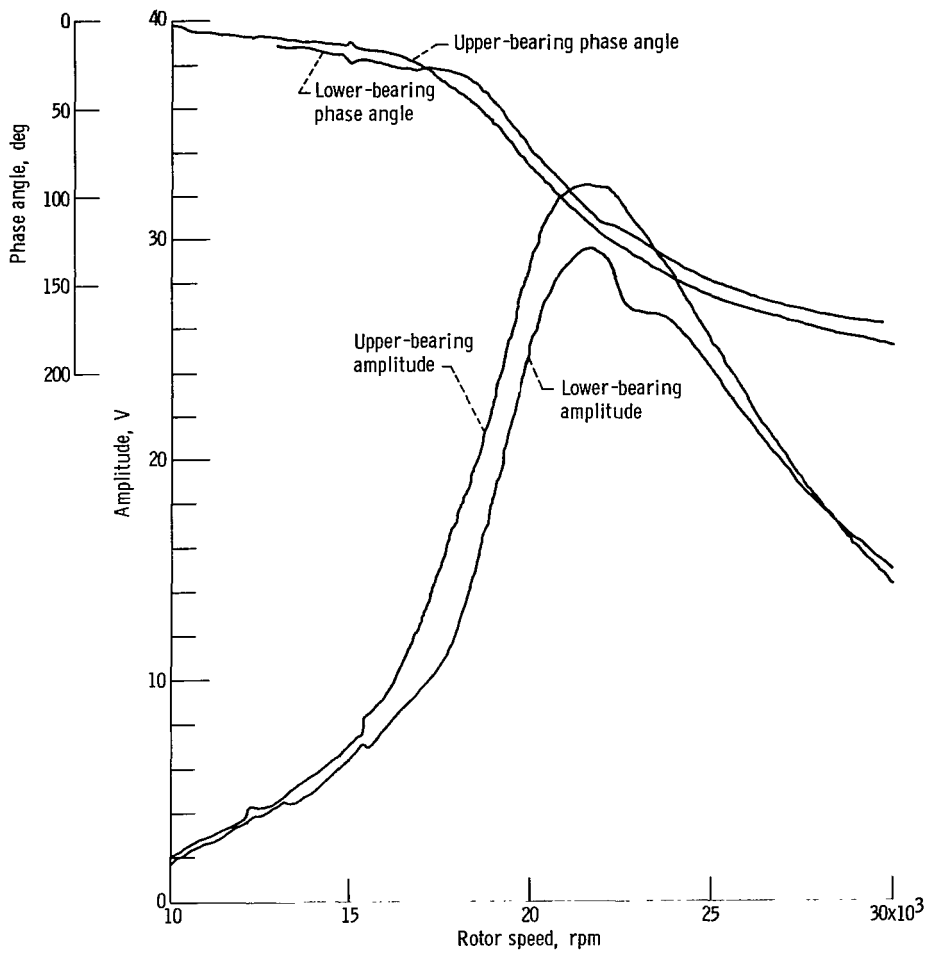

Figure 5. - Plotter output of rotor amplitude and phase angle. Supply pressure ratio, 4.8; total unbalance, 52 g mm.

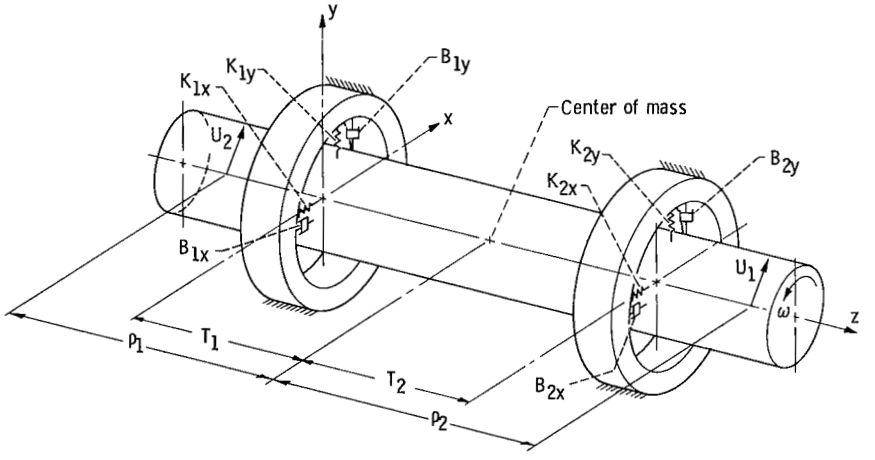

Figure 6. - Schematic diagram of rotor in bearings.

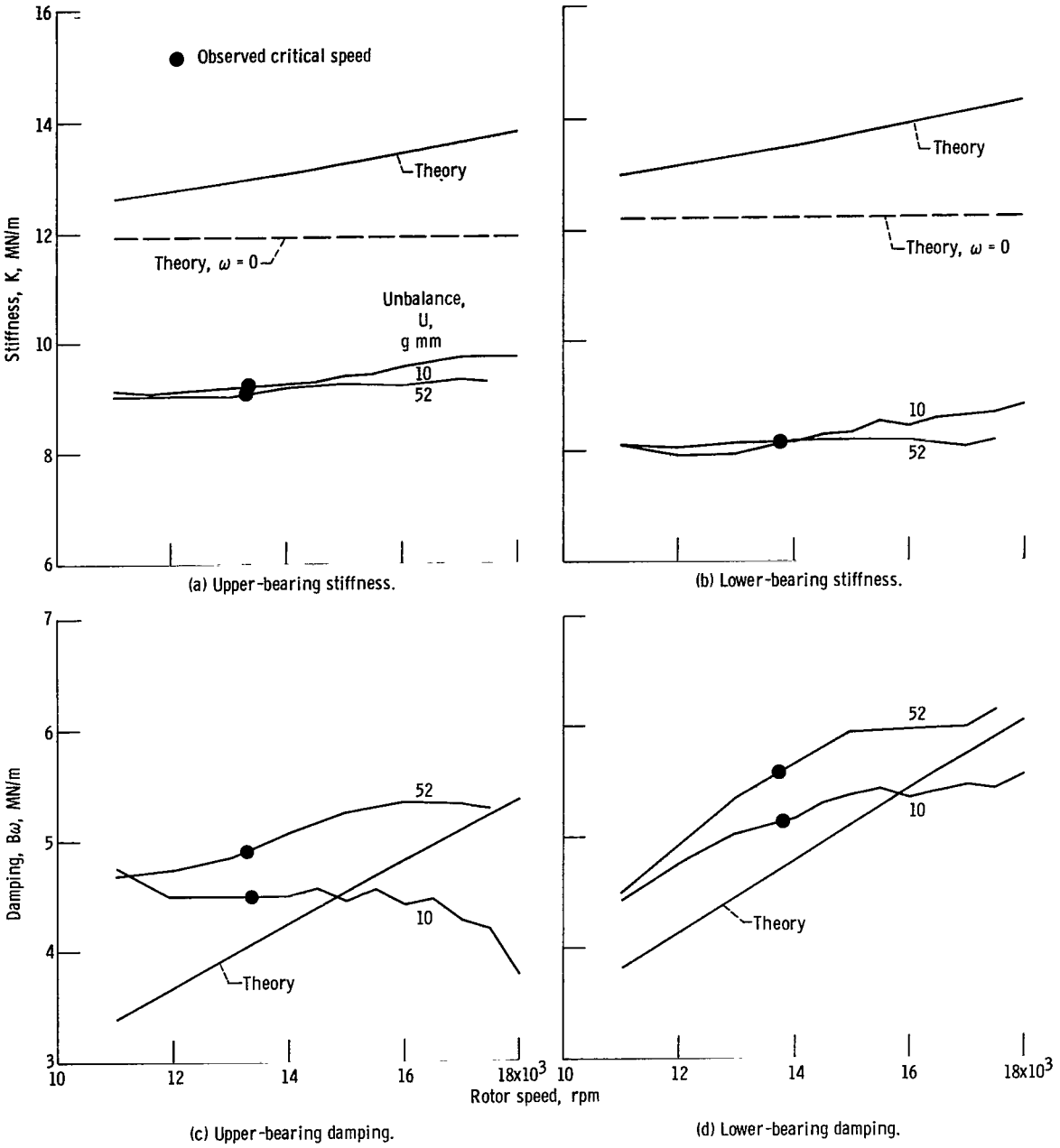

Figure 7. - Stiffness and damping of externally pressurized bearing with supply pressure ratio of 2.3.

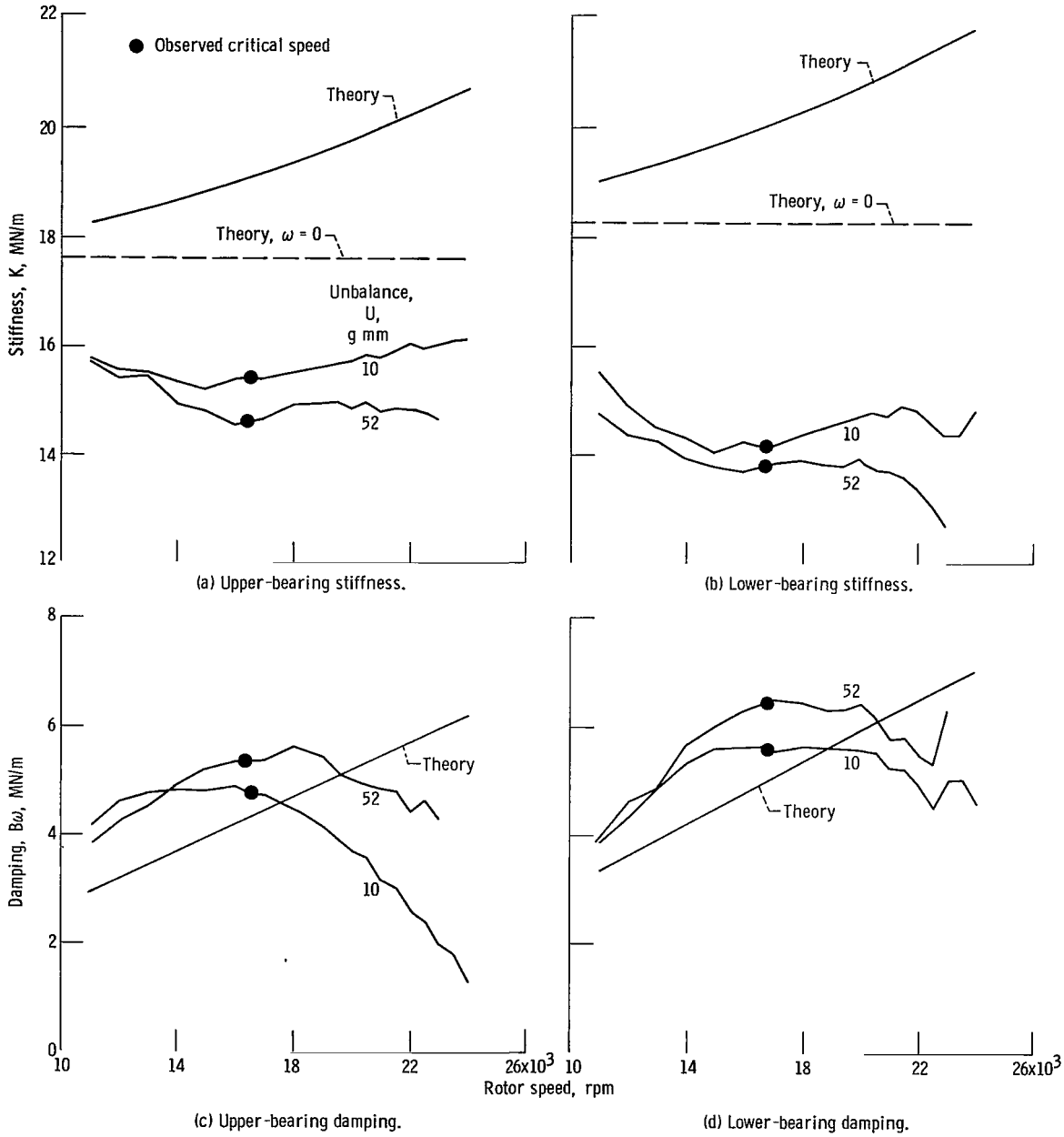

Figure 8. - Stiffness and damping of externally pressurized bearing with supply pressure ratio of 3.0.

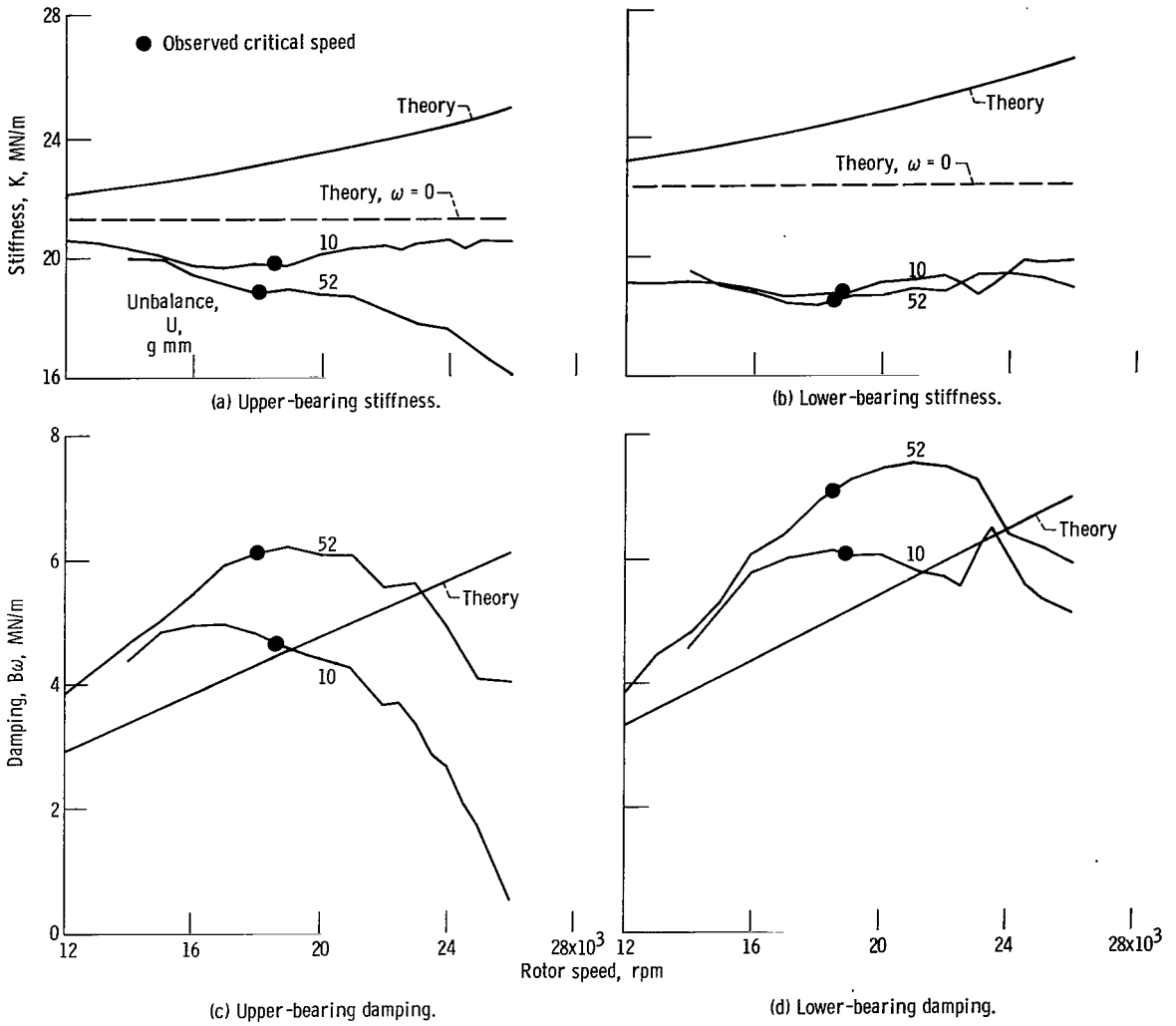

Figure 9. - Stiffness and damping of externally pressurized bearing with supply pressure ratio of 3.5.

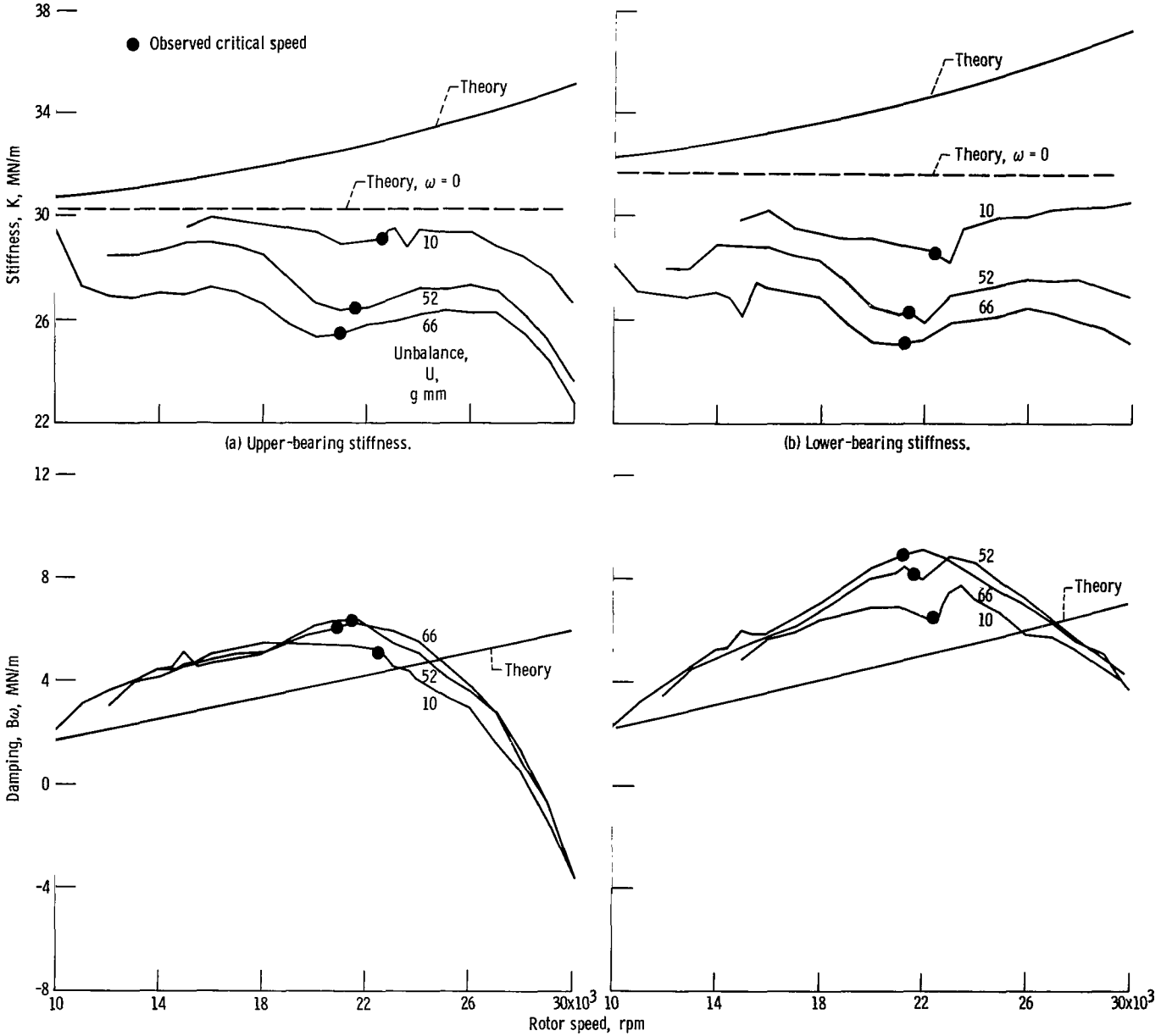

Figure 10. - Stiffness and damping of externally pressurized bearing with supply pressure ratio of 4.8.

"The aeronautical and space activities of the United States shall be conducted so as to contribute . . . to the expansion of human knowledge of phenomena in the atmosphere and space. The Administration shall provide for the widest practicable and appropriate dissemination of information concerning its activities and the results thereof."

—NATIONAL AERONAUTICS AND SPACE ACT OF 1958

NASA SCIENTIFIC AND TECHNICAL PUBLICATIONS

TECHNICAL REPORTS: Scientific and technical information considered important, complete, and a lasting contribution to existing knowledge.

TECHNICAL NOTES: Information less broad in scope but nevertheless of importance as a contribution to existing knowledge.

TECHNICAL MEMORANDUMS: Information receiving limited distribution because of preliminary data, security classification, or other reasons. Also includes conference proceedings with either limited or unlimited distribution.

CONTRACTOR REPORTS: Scientific and technical information generated under a NASA contract or grant and considered an important contribution to existing knowledge.

TECHNICAL TRANSLATIONS: Information published in a foreign language considered to merit NASA distribution in English.

SPECIAL PUBLICATIONS: Information derived from or of value to NASA activities. Publications include final reports of major projects, monographs, data compilations, handbooks, sourcebooks, and special bibliographies.

TECHNOLOGY UTILIZATION PUBLICATIONS: Information on technology used by NASA that may be of particular interest in commercial and other non-aerospace applications. Publications include Tech Briefs, Technology Utilization Reports and Technology Surveys.

Details on the availability of these publications may be obtained from:

SCIENTIFIC AND TECHNICAL INFORMATION OFFICE

NATIONAL AERONAUTICS AND SPACE ADMINISTRATION

Washington, D.C. 20546